Korean J. Chem. Eng.
DOI: 10.1007/s11814-021-1013-z

pISSN: 0256-1115
eISSN: 1975-7220

Nano-sized hematite-assembled carbon spheres for effectively adsorbing paracetamol in water: Important role of iron

Ton That Loc*,, Nguyen Duy Dat***, and Hai Nguyen Tran*,**,†**

*Institute of Fundamental and Applied Sciences, Duy Tan University, Ho Chi Minh City, 700000, Vietnam
**Faculty of Environmental and Chemical Engineering, Duy Tan University, Da Nang, 550000, Vietnam
***Faculty of Chemical & Food Technology, Ho Chi Minh City University of Technology and Education, Thu Duc, Ho Chi Minh City, 700000, Vietnam
(*Received 25 September 2021 • Revised 7 November 2021 • Accepted 11 November 2021*)

Abstract−This study developed a new α-Fe_2O_3 (hematite) nanoparticles-loaded spherical biochar (H-SB) through the direct pyrolysis of glucose-derived spherical hydrochar and $FeCl_3$. The optimal impregnation ratio (hydrochar and $FeCl_3$) was 1/1.25 (wt/wt). H-SB was applied to remove paracetamol (PRC) from water. Results indicated that H-SB exhibited a relatively low surface area (127 m^2/g) and total pore volume (0.089 cm^3/g). The presence of iron particles in its surface was confirmed by scanning electron microscopy with energy dispersive spectroscopy. The dominant form of iron nanoparticles (α-Fe_2O_3) in its surface was confirmed by X-ray powder diffraction and Raman spectrum. The crystallite size of α-Fe_2O_3 in H-SB was 27.4 nm. The saturation magnetization of H-SB was 6.729 emu/g. The analysis of Fourier-transform infrared spectroscopy demonstrated that the C-O and O-H groups were mainly responsible for loading α-Fe_2O_3 nanoparticles in its surface. The adsorption study indicated the amount of PRC adsorbed by H-SB slightly decreased within solution pH from 2 to 11. The adsorption reached a fast saturation after 120 min. The Langmuir maximum adsorption capacity of H-SB was 49.9 mg/g at 25 °C and pH 7.0. Ion-dipole interaction and π-π interaction played an important role in adsorption mechanisms, while hydrogen bonding and pore filling were minor. Therefore, H-SB can serve as a promising material for treating PRC-contaminated water streams.

Keywords: Adsorption, Hematite, Ion-dipole Interaction, Nanoparticle, Paracetamol, Spherical Biochar

INTRODUCTION

Nanotechnological application using iron oxides or iron oxide-based on materials for water treatment has attracted much interest from researchers [1,2]. However, the size of those materials is in the nano range, so to some extent it has some limitations and health concern-related problems [3]. Therefore, it is necessary to load iron oxides in the surface of the materials. In the literature, carbonaceous porous materials—activated carbon (AC) and biochar—have been used as carrier for developing iron oxides-loaded composites. For example, Zhang et al. [4] developed the Fe_xO_y/biochar composite from banana peel and $FeSO_4$ through a two-stage process. The first process was the preparation of non-spherical biochar through pyrolysis at 600 °C. The second process was modified Fe_xO_y on the surface of the biochar by simply mixing with $FeSO_4$. The Fe_xO_y/biochar composite (83.6 mg/g) exhibited an outstanding adsorption capacity to methylene blue dye compared to pristine biochar (40.19 mg/g). Two-stage preparation of the iron oxide (Fe_3O_4)/activated carbon composite has been also reported by Jain and coworkers [5]. The first process involved the generation of AC through a chemical activation method. The composite was secondly prepared through the co-precipitation method of two salts ($FeCl_3 \cdot 6H_2O$ and $FeSO_4 \cdot 7H_2O$) in the surface of AC. The maximum adsorption capacity of the composite (3.2, 2.15, and 8.06 mg/g) towards Cu(II), Cd(II), and Cr(VI) was slightly higher than that of Fe_3O_4 (2.7, 0.09, and 5.5 mg/g, respectively). A similar two-stage preparation of the iron oxide/activated carbon composite was successfully published by Kaur and colleagues [6].

Unlike traditional non-spherical biochar and non-spherical AC (according to their surface morphology), innovative spherical biochar and AC exhibited several outstanding properties, such as higher content of oxygen functional groups. This is because the feedstocks used for preparing non-spherical biochar are completely different from those for spherical biochar. In general, non-spherical biochar is usually prepared from lignocellulosic materials (i.e., pomelo peels and banana peels) through a pyrolysis process without using any activating chemicals (i.e., KOH) [4,7]. In contrast, spherical biochar is often synthesized from pure carbohydrate sources (i.e., glucose, xylose, starch, and sucrose) [7-9]. Because carbohydrates are well dissolved in water, a preliminary treatment using a hydrothermal carbonization technique is often applied to obtain a certain solid, known as spherical hydrochar. The formation mechanism of spherical hydrochar under the hydrothermal carbonization has been reported by Sevilla and Fuertes [10] and described in Fig. S1(a). The spherical carbons (spherical hydrochar, biochar, and activated carbon) exhibit a core-shell structure (Fig. S1(b)). Each particle of spherical carbons consists of a hydrophobic core and hydrophilic shell. The hydrophobic core contains a highly aromatic nucleus with oxygen-carrying functional groups (i.e., pyrone, quinone, and ether). In contrast, the hydrophilic shell comprises the

†To whom correspondence should be addressed.
E-mail: trannguyenhai@duytan.edu.vn, trannguyenhai2512@gmail.com
Copyright by The Korean Institute of Chemical Engineers.

high density of oxygen-containing functional groups such as carboxylic, carbonyl, and hydroxyl/phenolic (Fig. S1(b)) [9,10]. Those groups often play an essential role in adsorbing various pollutants in water [9,11]. In the literature, most studies often focus on developing composites based on traditional non-spherical biochar and AC. Thus, there is still a limitation on using spherical biochar as a carrier for loading iron nanoparticles.

Along with traditional pollutants (i.e., organic dyes and potentially toxic metals), the ubiquitous occurrence of emerging contaminants (i.e., pharmaceuticals, personal care products, and endocrine disruptors) in water environments has drawn some urgent attention [7,12]. This is because of their adverse effects on human health and the aquatic ecosystem [13,14]. Among current emerging contaminants, paracetamol (PRC; also known as N-acetyl-p-aminophenol, 4-acetamidophenol, or acetaminophen) is usually detected in municipal wastewater [15,16]. This is because of its frequent utilization in hospitals and households (especially in developing countries) for effectively treating various symptoms such as headaches, toothaches, backaches, osteoarthritis, and fever [15-18].

According to the report of research and markets regarding "Paracetamol Market-Growth, Trends, COVID-19 Impact, and Forecasts (2021-2026)" [19], the COVID-19 (coronavirus disease) pandemic has had an enormous impact on the Global paracetamol market (both its production and demand). This is because the paracetamol drug is often used for the early treatment of COVID-19-infected patients, especially in home treatment [20]. The compound annual growth rate for industry growth analysis is 4.3% (for the study period of 2018-2026) and 0.7% (2020-2026) [19]. The trend of paracetamol market is anticipated to increase from 750.5 million US dollars in 2020 to 788.5 million US dollars by 2026 [19].

As common analgesic drugs, PRC is frequently used in overdose [21]. As a result, the PRC residuals excreted from the user's body can be discharged into municipal wastewater. Le et al. [22] reported that the levels of PRC measured in the aquatic streams (municipal wastewater, treated wastewater, surface water, and drinking water) were remarkably higher than those of pharmaceutical products. For example, the concentration of PRC (45-163 μg/L) in municipal wastewater exceeded that of naproxen (0.9-321 μg/L), ibuprofen (0.28-6.1 μg/L), diclofenac (0.46-4.41 μg/L), and salicylic (0.9-1.48 μg/L). PRC has been detected in European groundwater [23]. Nunes [24] evaluated the toxicity of PRC toward biota and ecosystem and concluded that the presence of PRC residuals had a strongly negative impact on wild environments even at low PRC concentration. However, its effects are not confined to oxidative stresses, antioxidant defenses, and peroxidative damages. Other traits are also involved including ecotoxicological effects including histological development, tissue regeneration, embryogenesis and development, metabolism, and neurotoxicity and behavior [24]. This means that the ecotoxicological effects of PRC are hard to confirm appropriately. Although the exposure of emerging organic compounds (i.e., pharmaceuticals) in water environment (under trace levels) does not cause acute toxic effects, their accumulation and long-term exposure can threaten aquatic ecosystems and increase the risk to human health [7,14]. This phenomenon is commonly known as a potential cocktail effect [23]. Therefore, removing PRC from water is essential for protecting human health and the environmental ecosystem.

This study takes advantage of the change of iron salt (i.e., $Fe(NO_3)_3$ or $FeCl_3$) under different temperatures into various kinds of iron oxides to develop a new iron nanoparticle-loaded adsorbent [25-27]. The α-Fe_2O_3 (hematite) nanoparticles-loaded spherical biochar (H-SB) was direly prepared by a one-step carbonization process using spherical hydrochar and $FeCl_3$. Spherical hydrochar was first prepared through the hydrothermal carbonization process of glucose. The SB material was well characterized by textural property, surface morphology and element component, crystalline structure, surface functionality, magnetism, and electrical state. The process of paracetamol removal was conducted under batch experiments to explore the adsorption kinetics, isotherm, and thermodynamics. The effect of pH solution on the adsorption process was additionally examined. The adsorption mechanism was also discussed herein.

MATERIALS AND METHOD

1. Materials

Commercial α-D-glucose ($C_6H_{12}O_6$; its molecular weight (M_w) of 181.2 g/mol) that was purchased from Sigma-Aldrich was used as the pure carbohydrate source for generating carbon sphere. Iron (III) chloride hexahydrate ($FeCl_3{\cdot}6H_2O$; M_w=270.3 g/mol) was bought from Merch. Acetaminophen (or paracetamol; $CH_3CONHC_6H_4OH$; M_w=151.2 g/mol) was supplied from Sigma-Aldrich. Some other chemicals (i.e., NaOH, HCl, and NaCl) were acquired from Scharlau. These chemicals were direly used without additional purification.

2. Synthesis of Spherical Hydrochar, Spherical Biochar, and Hematite-assembled Spherical Biochar

Spherical hydrochar was synthesized from glucose through a hydrothermal carbonization method [11]. Briefly, approximately 15 g glucose was immersed into 120 mL deionized water and then trans- ferred into a Teflon autoclave (its total volume of 150 mL). The autoclave was placed in an oven and the temperature in the oven was maintained at 190 °C for 24 h. The precipitated solids (denoted as spherical hydrochar; SH) after the hydrothermal carbonization were washed and dried at 105 °C for 24 h.

Hematite-assembled spherical biochar (H-SB) was prepared from SH and $FeCl_3$ through a pyrolysis process at 400 °C for 3 h. The impregnation ratio of SH and $FeCl_3$ (wt./wt.) was 1/0, 0.5/1, 1/1, 1/1.25, 1/1.5, and 1/2.0. The primary study (data not shown) indicated that the material prepared at the impregnation ratio of 1/1.25 exhibited the highest adsorption capacity of paracetamol in water. Therefore, the H-SB material prepared at this ratio was characterized and applied for removing PRC from water. After the pyrolysis process, H-SB was washed repeatedly with hot deionized water and then dried at 105 °C for 24 h. The material prepared at the impregnation ratio of 1/0 (without using the $FeCl_3$ salt) was denoted as the pristine spherical biochar (SB) and used for comparisons (i.e., characteristics and adsorption capacity).

3. Characterization of the Prepared Materials

Nitrogen adsorption/desorption isotherm at 77 K was recorded by a PMI BET-Sorptometer. The textural properties of the materials were obtained from N_2 physisorption isotherms. Scanning elec-

tron microscopy and energy dispersive spectroscopy (SEM-EDS; JSM-6510 LV) were employed for assessing their surface morphology and main surface elements. The crystalline structure of iron oxides on the spherical biochar was identified by X-ray diffractometer (XRD; D6 Advance Bruker) and Raman technique (Xplora Plus; HORIBA). Fourier-transform infrared spectroscopy (FTIR; IR Nicolet iS10) was applied to determine the main functionalities on their surface. Magnetic nature of H-SB was ascertained through EZ9MicroSense vibrating sample magnetometer at ~300 K with a magnetic field from −60 to +60 kOe.

4. Batch Adsorption Experiments

The operation conditions for removing PRC from water were carried out in batch adsorption experiments including different solution pH value, contact time, temperature, and initial PRC concentration. The solid/liquid ratio (m/V) in Eqs. (1)-(2) was kept at approximately 2.0 g/L. For the investigation of solution pH values, PRC concentration (~300 mg/L) was experienced in a pH range from 2.0 to 11, maintaining the other operation conditions such as 24 h and 25 °C. The adsorption kinetics, two initial PRC concentrations (517 and 883 mg/g at pH 7.0) were used, and the internal time was taken from 2.0 to 350 min at 25 °C. The adsorption isotherm was conducted at different initial PRC concentrations from 50 to 1,000 mg/L under pH 7.0, 25 °C, and the contact time of 24 h. The adsorption thermodynamics was examined as the adsorption isotherm, but different to temperatures such as 25 °C and 50 °C.

The PRC contaminant in solution was analyzed by high-performance liquid chromatograph (Dionex 3000 Thermo, Sunnyvale, California, USA) coupled with a photo-diode array [7]. Each adsorption experiment was repeated in triplicate and the value was reported as average±standard deviation. The amounts of PRC adsorbed by the prepared material at the equilibrium (q_e) and at any time (q_t) were computed as the following equations:

$$q_e = \frac{C_o - C_e}{m} \times V \quad (1)$$

$$q_t = \frac{C_o - C_t}{m} \times V \quad (2)$$

where C_o, C_t, and C_e (mg/L) are the concentrations of paracetamol in solution at the starting, at any time (t), and at the equilibrium, respectively; m (g) is the dry mass of the material; and V (L) is the volume of the PRC solution.

To evaluate the feasibility of using H-SB as a catalyst (~1.0 g/L), PRC degradation under the addition of H_2O_2 was studied. The ratio of [H_2O_2] to [RPC] was 10 : 1. The solution pH values were adjusted at 2.0, 5.0, and 7.0 during the removal processes (adsorption and degradation). The concentration of PRC after adsorption equilibrium was approximately 12 mg/L. The results (data not shown) indicated that degradation efficiency was negligible. The result suggested that the α-Fe_2O_3 solids on the surface of H-SB did not act as a Fenton-like catalyst.

RESULTS AND DISCUSSION

1. Characteristics of the Hematite-assembled Spherical Biochar

1-1. Surface Morphology and Element Component

The morphology and main element components on the H-SB's surface were observed by SEM images and EDS data (Fig. 1). Fig. 1(a) shows that H-SB has a spherical morphology similar to other spherical biochars [9] and spherical activated carbons [11] in the

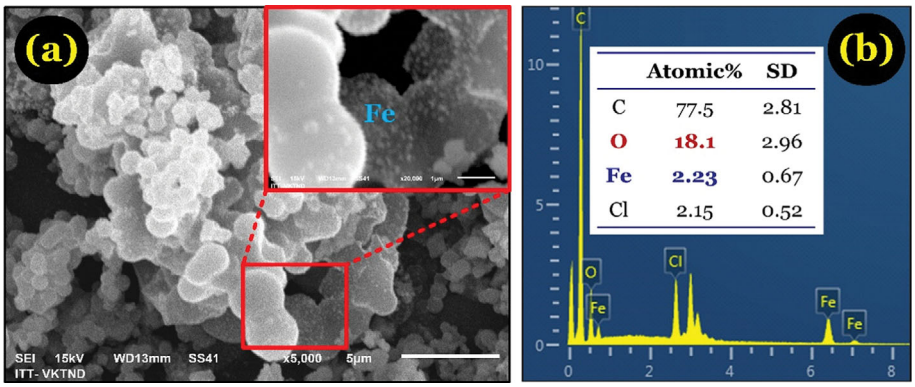

Fig. 1. (a) SEM and (b) EDS of the hematite-loaded spherical biochar (H-SB).

Table 1. Textural properties of the spherical hydrochar (SH), hematite-loaded spherical biochar (H-SB), and spherical biochar (SB)

	Abbreviation	Unit	Value		
			SH	H-SB	SB
BET surface area	S_{BET}	m^2/g	8.14	127	39.5
t-Plot micropore area	V_{Micro}	m^2/g	-	98.9	25.8
External surface area	V_{Ext}	m^2/g	-	28.4	13.7
Total pore volume	V_{Total}	cm^3/g	0.006	0.089	0.031
t-Plot micropore volume	V_{Micro}	cm^3/g	-	0.049	0.004

literature. Many interconnected spherical microparticles were directly observed through the SEM images. As expected, both SEM and EDS data confirmed the presence of Fe on the surface of H-SB. However, they did not provide information on the kinds of Fe (Fe_2O_3 or Fe_3O_4, etc.).

1-2. Textural Property

The textural properties of the adsorbents are listed in Table 1. The feedstock (glucose-derived spherical hydrochar; SH) exhibited a low Brunauer-Emmett-Teller (BET) surface area (S_{BET}=8.14 m^2/g) and total pore volume (V_{Total}=0.006 cm^3/g). A similar result was found for other spherical hydrochars derived from sucrose (0.985 m^2/g and 0.003 cm^3/g) and xylose (5.912 m^2/g and 0.011 cm^3/g) [9]. The pyrolysis process of SH without the presence of $FeCl_3$ at 400 °C (for the spherical biochar; SB) led to increasing its S_{BET} value to 39.5 m^2/g and V_{Total} to 0.031 cm^3/g. However, the presence of $FeCl_3$ during the pyrolysis promoted considerably the textural properties of the resultant biochar (H-SB) up to 127 m^2/g for S_{BET} and 0.089 cm^3/g for V_{Total}. However, those materials (SH, SB, and H-SB) exhibited remarkably lower S_{BET} and V_{Total} values than commercial activated carbon (CAC; 1,284 m^2/g and 0.680 cm^3/g) [15], non-spherical AC (1,202 m^2/g and 1.09 cm^3/g) [17], and spherical ACs (801-1,612 m^2/g and 0.47-0.86 cm^3/g) [11]. In addition, Sui et al. [28] reported the low S_{BET} and V_{Total} values of pure α-Fe_2O_3 were 36.5 m^2/g and 0.010 cm^3/g, respectively. Therefore, the contribution of pore filling to adsorbing PRC drug in water was not as much important as other adsorption mechanisms (i.e., π-π interaction).

1-3. Crystalline Structure

Like activated carbon and non-spherical biochar, spherical biochar is commonly classified as an amorphous material [7,9]. Therefore, the crystal nature of H-SB (detected by the XRD spectrum) resulted from the presence of certain iron oxides on its surface.

It is necessary to distinguish crystallinities among α-Fe_2O_3 (hematite), γ-Fe_2O_3 (maghemite), and Fe_3O_4 (magnetite). Fig. S2 provides a comparison of the XRD spectrum of different kinds of iron oxides (i.e., γ-Fe_2O_3, α-Fe_2O_3, and Fe_3O_4 nanoparticles) in the literature [29] and in this study. The result suggests that the XRD spectrum of H-SB (Fig. 2 or Fig. S2(d)) displays many peaks corresponding to the crystallinity of α-Fe_2O_3 nanostructures (Fig. S2(b)) and similar to the standard PDF card (JCPDS No. 33-0664). The relevant peaks in the XRD spectrum (Fig. 2) are similar to those reported elsewhere [26,28-34]. Therefore, it can be concluded that the $FeCl_3$ salt was mainly converted to α-Fe_2O_3 nanoparticles on the spherical biochar under pyrolysis ($FeCl_3$ and SH) at 400 °C [25,27]. Similarly, Cao et al. [26] investigated the transformation of $Fe(NO_3)_3 \cdot 9H_2O$ under different calcination temperatures. They reported that γ-Fe_2O_3 was formed within the range of calcination temperature of 130-200 °C, both γ-Fe_2O_3 and α-Fe_2O_3 were at the range of 200-400 °C, and α-Fe_2O_3 was at temperature >500 °C.

Furthermore, the Scherrer equation was applied to estimate the crystallite size of α-Fe_2O_3 on the surface of H-SB. The values of the intense peaks related to the (104) and (110) planes were used for calculating [28]. The result showed that the crystallite size of α-Fe_2O_3 in H-SB was 27.4±2.31 nm, similar to alone α-Fe_2O_3 [34] (21.8±1.22 nm in Fig. 2). Similarly, Fouad et al. [31] reported that the crystallite size (determined by XRD) and particle size (calculated based on transmission electron microscopy) of α-Fe_2O_3 synthesized by the precipitation method were 14-26 nm and 16-44 nm, respectively. A lager crystallite size of α-Fe_2O_3 (33 nm) and (60-64 nm) was reported by Ahmmad et al. [30] and Dar and Shivashankar [29], respectively.

The combination structure of spherical biochar and α-Fe_2O_3 particles was clearly identified by the Raman technique (Fig. 3). The typical characteristics involved in the non-graphitic carbon material (H-SB) were confirmed by the presence of two peaks at approximately 1,305 cm^{-1} (denoted as a D band) and 1,574 cm^{-1} (G band). The intensity ratio of D and G bands (I_D/I_G) was 1.129. The I_D/I_G ratio of H-SB was lower than that of some carbon materials such as commercial activated carbon (I_D/I_G=2.011) [15], spherical biochar prepared at 900 °C (1.867) [7], and non-spherical biochar prepared at 700 °C (1.827) [7]. This is because the pyrolysis temperature (400 °C) used for generating H-SB was lower than that for the others [7].

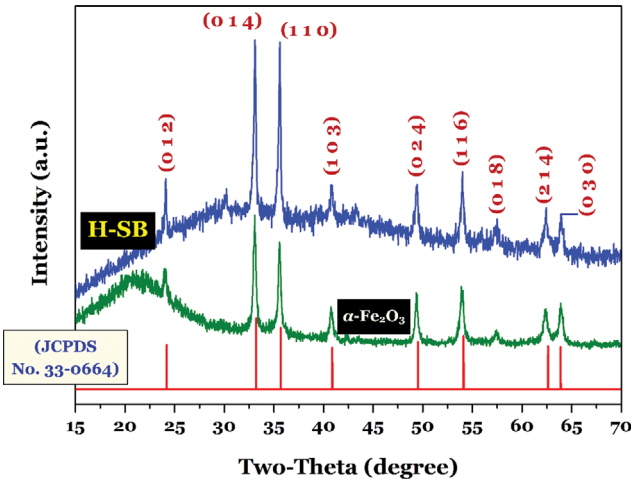

Fig. 2. XRD spectrum of the α-Fe_2O_3 synthesized from the co-precipitation method [34] and the hematite-loaded spherical biochar (H-SB).

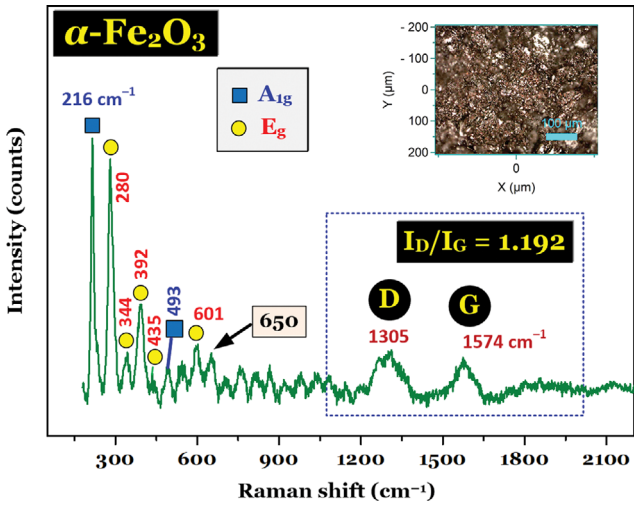

Fig. 3. Raman spectrum of the hematite-loaded spherical biochar (H-SB).

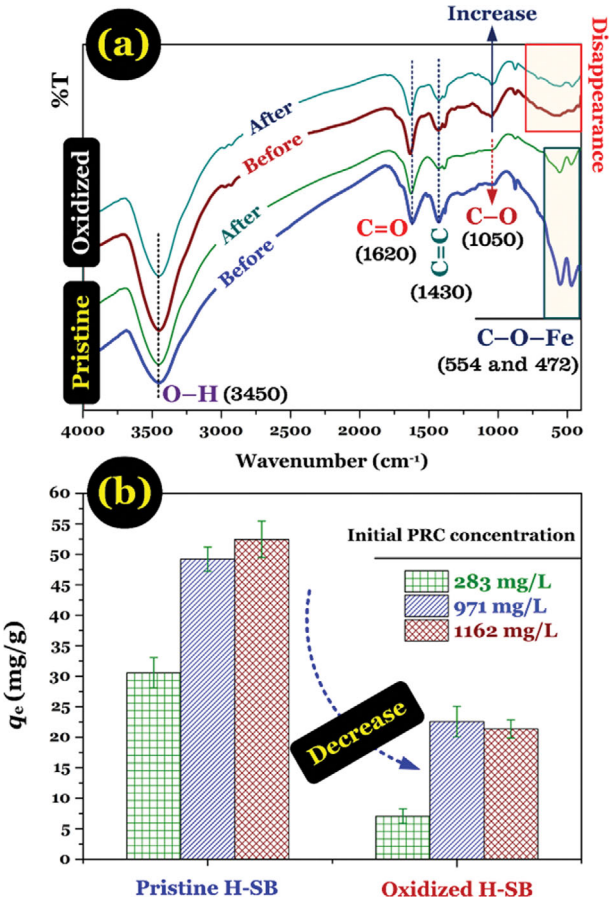

Fig. 4. (a) FTIR of the hematite-loaded spherical biochar (H-SB) and oxidized H-SB before and after adsorption, and (b) their adsorption capacities towards PRC at different initial PRC concentrations.

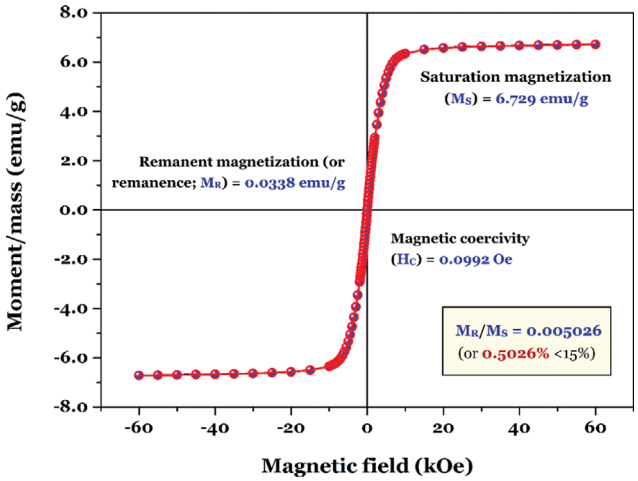

Fig. 5. Magnetic hysteresis loop of the hematite-loaded spherical biochar (H-SB) at ~300 K.

Furthermore, the presence of α-Fe_2O_3 in H-SB was confirmed by several phonon modes in the region of 150-1,000 cm^{-1} (Fig. 3). For example, two peak positions at around 216 cm^{-1} and 493 cm^{-1} belong to the A_{1g} phonon mode; meanwhile, five others (~280, 344, 392, 435, and 601 cm^{-1}) are related to the E_g phonon mode [30,31]. The peak at 650 cm^{-1} indicates the structural disorder in the crystal lattice of hematite (α-Fe_2O_3) [29,31]. The pattern of the Raman spectrum of H-SB is similar to that of the nanocomposites (derived from α-Fe_2O_3 nanostructures and reduced graphene oxides) [32], the prepared α-Fe_2O_3 nanoparticles in Fig. S3 [29] and in documents [31,33], and the commercial α-Fe_2O_3 nanoparticles [30].

The results suggest that the H-SB composite exhibited the important properties of their parents for adsorbing PRC in water. For example, it can adsorb organic contaminants (feasible for PRC) adequately through π-π interaction (based on the feature of spherical biochar) [7,9] and ion-dipole interaction (α-Fe_2O_3 nanoparticles) [14,35].

1-4. Surface Functionality

The functional groups on the surface of H-SB were identified through the analysis of FTIR spectrum. Fig. 4(a) depicts several important bands in H-SB. They include 3,450 cm^{-1} (the OH groups derived from phenolic and carboxylic), 1,620 cm^{-1} (C=O groups from lactonic and carboxylic), 1,430 cm^{-1} (C=C group from aromatic rings), 1,050 cm^{-1} (C-O group from lactones or ethers) [7, 11,15,17]. The presence of iron oxides in its surface was identified through the C-O-Fe group by two bands at 554 and 472 cm^{-1} [5,31]. FTIR data confirmed that the O-H and C-O groups were primarily responsible for binding iron oxides in the surface of H-SB. This conclusion will be further discussed in Section 2.5 (Feasible Adsorption Mechanisms).

1-5. Magnetic Characteristics

The magnetic properties of H-SB were measured through its magnetic hysteresis loop at 300 K (Fig. 5). The different shapes of hysteresis loops were introduced by Waters et al. [36] and summarized in Fig. S4. The magnetization curve in Fig. 5 indicates a typical S-shape, suggesting that H-SB exhibits the typical properties of a ferrimagnetic material [6].

In essence, the saturation magnetization (M_S) of the composites containing magnetic solids (i.e., α-Fe_2O_3) is strongly dependent on preparation method, particle size, morphological shape, ratios of chemicals (i.e., $FeCl_3$) and feedstock (i.e., carbon sphere), and temperature [6,31,33]. The M_S of H-SB was 6.729 emu/g, which is relatively similar to that of pure α-Fe_2O_3 nanoparticles (7.5 emu/g) and the magnetic nanocomposite of α-Fe_2O_3/activated carbon (5.6 emu/g) [37]. The coercivity (H_C; 0.0992 Oe) and remanence (M_R; 0.0338 emu/g) of H-SB were close to zero. This means that the characteristics of H_C and M_R were invisible in the plot of magnetization and magnetic field (Fig. 5). In addition, the ratio of M_R to M_S (M_R/M_S=0.5026%) was less than 15%. The results suggest that H-SB exhibits a superparamagnetic property [37].

2. Adsorption Performance

2-1. Effect of Solution pH Values on the Adsorption Process

The profile of pH-dependent adsorption is provided in Fig. 6. The pH_{PZC} of H-SB was 2.5. Thus, its surface charge was predominantly negative when solution pH ($pH_{solution}$) was higher than 2.5. The p*K*a of PRC was higher than 9.0 (i.e., 9.3 [38], 9.4 [17], 9.5 [18], and 9.8 [16]) because of the presence of the OH group in its molecules. Therefore, it exists as an uncharged organic molecule

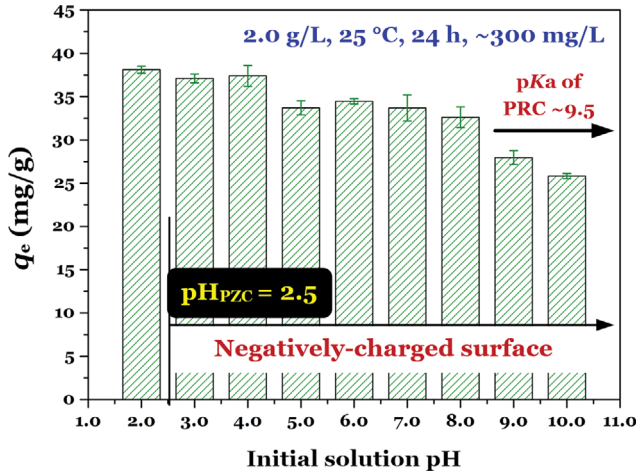

Fig. 6. Effect of solution pH on the adsorption capacity of the hematite-loaded spherical biochar (H-SB) towards PRC in solution.

when $pH_{solution}$< its p*K*a. As a result, electrostatic attraction might play a less important role in absorbing PRC into H-SB.

In general, the adsorption capacity of H-SB slightly decreased by approximately 14% when $pH_{solution}$ increased from 2.0 to 8. When solution pH ($pH_{solution}$ from 9 to 10) was nearly the p*K*a of PRC, its adsorption capacity decreased by 21% (from 32.61 mg/g at pH 8 to 25.8 mg/g at pH 10) because of electrostatic repulsions between the negatively charged sites on the H-SB's surface and PRC anions in solutions. A decrease in PRC adsorption efficiency within increasing $pH_{solution}$ was reported by Spessato and co-workers [18]. This might be because of competition between the OH^- anions in solution and PRC for the absorbing sites available on the surface of H-SB [13]. Another reason might result from aggregating PRC molecules to form its dimers [39].

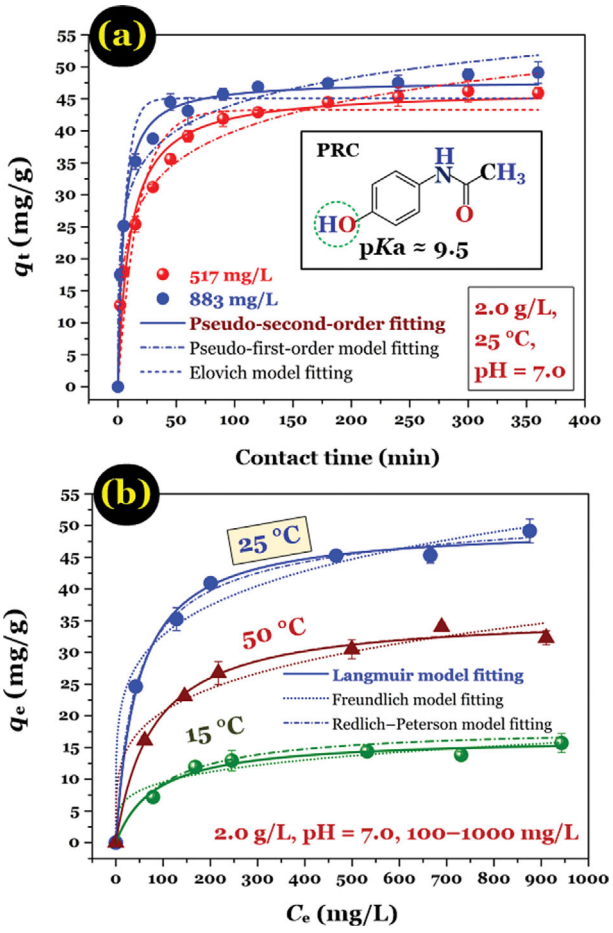

Fig. 7. (a) Adsorption kinetics and (b) isotherm of PRC onto the hematite-loaded spherical biochar (H-SB).

2-2. Adsorption Kinetics

The time-dependent profile for PRC adsorption at two initial concentrations of PRC (C_o=517 and 883 mg/L) is presented in Fig. 7(a). Generally, an increase in the initial concentration slightly enhances the amount of PRC adsorbed by H-SB and adsorption equilibrium duration. The adsorption process reached an equilibrium after a 120-min contact. Fast adsorption equilibrium might be attributed to the surface adsorption phenomenon; the adsorption process mainly occurred on the surface of H-SB. This means that pore-filling roles in the adsorption mechanism of PRC by H-SB (S_{BET}=127.3 m^2/g and V_{Total}=0.089 cm^3/g) were less important than those by several other carbonaceous porous materials such as CAC (1,248 m^2/g and 0.680 cm^3/g) [15] and Kon-Tiki kiln-derived AC (845 m^2/g and 0.41 cm^3/g) [16].

In this study, three kinetic adsorption models were introduced to mathematically evaluate intrinsic adsorption constants: the pseudo-first order (PFO) model (Eq. (3)), pseudo-second-order (PSO) model (Eq. (4)), and Elovich (Eq. (5)) model. Those models have been widely applied for modeling various kinetic adsorption processes in solid-liquid phases [13,15,17].

$$q_t = q_e[1-\exp(-k_1 t)] \quad (3)$$

$$q_t = \frac{q_e^2 k_2 t}{1+q_e k_2 t} \quad (4)$$

Table 2. Parameters of the models of selective adsorption kinetics of PRC onto H-SB

	Unit	Initial PRC concentration	
		517 mg/L	883 mg/L
1. Pseudo-first-order model			
q_e	mg/g	43.3	45.1
k_1	1/min	0.057	0.156
adj-R^2	—	0.923	0.933
red-χ^2	—	16.8	14.7
2. Pseudo-second-order model			
q_e	mg/g	46.4	47.9
k_2 ($\times 10^3$)	g/(mg·min)	2.09	4.50
adj-R^2	—	0.975	0.986
red-χ^2	—	5.38	3.16
3. Elovich model			
α	mg/(g·min)	20.4	96.5
β	mg/g	0.142	0.167
adj-R^2	—	0.985	0.979
red-χ^2	—	3.25	4.57

$$q_t = \frac{1}{\beta}\ln(1+\alpha\beta t) \quad (5)$$

where q_t and C_t have been defined in Eq. (2); k_1 (1/min) is the adsorption rate constant of the PFO model; k_2 [g/(mg·min)] is the adsorption rate constant of the PFO model; α [mg/(g·min)] is the initial rate constant of the Elovich equation; and β (g/mg) is the desorption constant during any one experiment.

The relevant parameters of the selected models that were calculated by the optimization method of non-linearization are summarized in Table 2. The result shows that three target models can well describe the relevant experiment data. Based on the criteria of high adjust determination coefficient (adj-R^2) and low reduced chi-squared (red-χ^2) value, the fitting order of the models was the Elovich model (0.979-0.985 and 3.25-4.57)>the PSO model (0.975-0.986 and 3.16-5.38)>the PFO model (0.923-0.933 and 14.7-16.8, respectively).

Table 2 shows that the initial rate constant α of the Elovich model was 20.4 and 96.5 mg/(g·min) corresponding to the initial PRC concentration of 517 mg/L and 883 mg/L, respectively. A simar tendency was obtained for the PSO rate constant as follows: 2.09×10^{-3} at C_o=517 mg/L and 4.50×10^{-3} at C_o=883 mg/L. This means that an increase in the initial PRC concentration led to increasing the adsorption rate constant. The result suggests the presence of driving force in the adsorption system.

2-3. Adsorption Isotherms

The profiles of PRC adsorption isotherms at different solution temperatures (10 °C, 25 °C, and 50 °C) are depicted in Fig. 7(b). Three common adsorption isotherms that were used for modeling the equilibrium adsorption data were the Langmuir model (Eq. (6)), Freundlich model (Eq. (7)), and Redlich-Peterson model (Eq. (8)) [4,6,17,34].

$$q_e = \frac{Q_{max}K_LC_e}{1+K_LC_e} \quad (6)$$

$$q_e = K_FC_e^{n_F} \quad (7)$$

$$q_e = \frac{K_{RP}C_e}{1+a_{RP}C_e^g} \quad (8)$$

where q_e and C_e are previously defined in Eq. (1); Q_{max} (mg/g) is the Langmuir maximum adsorption capacity of H-SB toward PRC; K_L (L/mg) is the Langmuir equilibrium constant; K_F [(mg/g)/(L/mg)^{n_F}] is the Freundlich constant; n_F (dimensionless; 0<ng<1) is a Freundlich intensity parameter; K_{RP} (L/g) is the Redlich-Peterson constant; a_{RP} (L/mg)^g is the Redlich-Peterson equilibrium constant; and g (dimensionless; 0<g<1) is the exponent of the Redlich-Peterson model.

The modeling results are provided in Table 3. The equilibrium adsorption data were adequately described by the Langmuir model (0.980-0.995 for adj-R^2 and 0.61-1.57 for red-χ^2) than the Redlich-Peterson model (0.928-0.995 and 1.06-2.18) and the Freundlich model (0.948-0.981 and 1.57-5.49, respectively). The exponent g (0.949-0.999) of the Redlich-Peterson was close to unity, additionally confirming the Langmuir model was better than the Freundlich one in describing the behavior of PRC adsorption by H-SB.

Clearly, the adsorption process is strongly dependent on the opertaional temperatures (Fig. 6(b)). When the temperature increased from 15 °C to 25 °C, the Langmuir maximum adsorption capacity of H-SB (Q_{max}) remarkably increased from to 16.6 mg/g to 49.9 mg/g. However, with a further increase in the temperature to 50 °C, its maximum adsorption capacity decreased to 36.0 mg/g. The adsorption tendencies are consistent with those described in previous research for adsorbing PRC by commercial AC [15] and different kinds of AC [40].

The maximum adsorption capacity of its feedstock (special hydrochar; SH) and pristine spherical biochar (without α-Fe_2O_3; SB) was also investigated. The result (data not shown) indicates that the Q_{max} value of SH (0.15 mg/g) and SB (3.51 mg/g) was remarkably lower than that of H-SB (49.9 mg/g) under the same experi-

Table 3. Parameters of the models of selective adsorption isotherm of PRC onto H-SB

	Unit	Solution temperature		
		15 °C	25 °C	50 °C
1. Langmuir model				
Q_{max}	mg/g	16.6	49.9	36.0
K_L	L/mg	0.012	0.022	0.013
adj-R^2	—	0.980	0.995	0.994
red-χ^2	—	0.61	1.57	0.844
2. Freundlich model				
K_F	(mg/g)/(mg/L)^n	3.41	13.4	7.04
n_F	—	0.224	0.194	0.234
adj-R^2	—	0.948	0.981	0.975
red-χ^2	—	1.57	5.49	3.53
3. Redlich-Peterson model				
K_{RP}	L/g	0.193	1.37	0.465
a_{RP}	(L/mg)^g	0.011	0.038	0.013
g	—	0.999	0.949	0.999
adj-R^2	—	0.928	0.995	0.993
red-χ^2	—	2.18	1.40	1.06

Table 4. Comparison of the Langmuir maximum adsorption capacity of paracetamol (Q_{max}; mg/g) by the H-SB material in this study and other previously referenced materials

Adsorbent	Its feedstock	Material preparation		Textural parameters		Q_{max} (mg/g)	Reference
		Pyrolysis temperature	Activation	S_{BET} (m^2/g)	V_{Total} (cm^2/g)		
Commercial AC	—	—	—	1,284	0.680	221	[15]
Activated carbon (AC)	Kon-Tiki kiln	900 °C	Physical (CO_2)	676	0.34	98.2	[16]
AC	spent tea leaves	600 °C	Chemical (H_3PO_4)	1,202	1.09	59.2	[17]
Biochar	**Glucose**	**350 °C**	**$FeCl_3$**	**127**	**0.089**	**49.9**	**This study**
AC	Orange peels	500 °C	Chemical (H_3PO_4)	-	-	28.1	[41]
Biochar	Softwood	550 °C	—	313	0.028	27.7	[12]
Biochar	Bamboo	315 °C	—	68.7	0.017	25.9	[12]
Biochar	Kon-Tiki kiln	700 °C	—	392	0.18	14.7	[16]

Table 5. Thermodynamic parameters of PRC adsorption onto H-SB obtained from different temperatures

T (K)	K_C	van't Hoff equation	Thermodynamic parameters		
			ΔG^o (kJ/mol)	ΔH^o (kJ/mol)	ΔS^o [J/(mol·K]
At three solution temperatures					
283	1,829	y=103489x+2005	−17.7	−860	16.7
298	3265	R^2=0.0008	−20.0		
323	1,954		−20.3		
At two solution temperatures					
283-298	—		—	27.1	158
298-323	—		—	−16.4	12.1

mental conditions. The result suggests the important role of nano iron oxides present in the surface of H-SB in adsorbing PRC molecules in water.

Table 4 provides a comparison of the maximum adsorption capacity of H-SB towards PRC and other materials in the literature. The Q_{max} value of H-SB (49.9 mg/g) was lower than that of commercial activated carbon (221 mg/g) [15] and some other prepared activated carbon (59.2-98.2 mg/g) [16,17]. This is because those AC materials were prepared at high pyrolysis temperature (600-900 °C), with further activation (chemical or physical) being required. However, H-SB still exhibited an excellent adsorption capacity compared to some other materials (14.7-28.1 mg/g; Table 4) [12,16,41].

2-4. Adsorption Thermodynamics

Three adsorption thermodynamic parameters (ΔG^o, ΔH^o, and ΔS^o) were calculated based on the equilibrium constant of the Langmuir model (K_L; L/mol). The standard Gibbs free energy change (ΔG^o) was directly calculated from Eq. (9). The van't Hoff equation is expressed as Eq. (10).

$$\Delta G^o = -RT\ln K_C \tag{9}$$

$$\ln K_C = \left(\frac{-\Delta H^o}{R}\right)\frac{1}{T} + \frac{\Delta S^o}{R} \tag{10}$$

where K_C (dimensionless) is the so-called thermodynamic equilibrium constant; R [8.3144 (J/mol·K)] is the universal gas constant, and T (K) is the solution temperature.

Table 5 displays the thermodynamic parameters for the PRC adsorption onto H-SB calculated based on three solution temperatures (283, 298, and 323 K). The negative ΔG^o values indicate that the adsorption occurred spontaneously without any further energy requirement.

Because the correlation coefficient (R^2=0.0008) of the van't Hoff equation (calculated based on three temperatures) was very low, the changes in standard enthalpy (ΔH^o) and standard entropy (ΔS^o) were calculated based on two solution temperatures. The ΔH^o value was computed from Eq. (11); meanwhile, the ΔS^o value was calculated as Eq. (12) [15].

$$\Delta H^o = R \times \ln\left(\frac{K_{C(2)}}{K_{C(1)}}\right) \times \frac{(T_1 \times T_2)}{(T_2 - T_1)} \tag{11}$$

$$\Delta G^o = \Delta H^o - T\Delta S^o \tag{12}$$

where $K_{C(1)}$ and $K_{C(2)}$ are the so-called thermodynamic equilibrium constant at T_1 and T_2, and T_1 and T_2 are the solution temperatures (T_1<T_2).

Table 5 indicates that the sign of ΔH^o is strongly dependent on the range of the investigated solution temperatures. This means that the adsorption process was endothermic (ΔH^o=27.1 kJ/mol within the solution temperatures of 283-298 K) and exothermic (ΔH^o= −16.4 kJ/mol within 298-323 K). Similarly, Nguyen et al. [15] concluded that the process of PRC adsorption by CAC occurred endothermically (ΔH^o=24.1 kJ/mol within 288-298 K) and exothermically

(ΔH^o=−6.36 kJ/mol within 298-323 K). An exothermic process (ΔH^o=−10.6 kJ/mol) was reported by Wong and colleague [17] for adsorbing PRC onto the AC developed from spent tea leaves.

The positive value for ΔS^o [158 and 12.1 J/(mol·K)] obtained at two temperatures (283-298 K and 298-323 K, respectively) suggests that the interface of adsorbent/adsorbate becomes more random during the adsorption process [15].

2-5. Feasible Adsorption Mechanisms

Adsorption mechanisms of aromatic pollutants by carbon materials often include various interactions. Table 1 shows that H-SB had a low S_{BET} value (127 m^2/g); thus, pore-filling mechanisms played a less important role in this study. In addition, the result of pH-dependent study (Section 2.1) indicated that electrostatic attraction did not substantially involve the adsorption process, especially at pH 7.0.

Hydrogen bonding interactions have been intensively reported in the literature as the main adsorption mechanism of aromatic pollutants (i.e., dye and PRC) onto certain materials. Those materials often exhibit abundant oxygen-containing functionalities in their surface. Such hydrogen bonding mechanisms might also exist in this adsorption process. Although the interactions played an integral role in adsorbing PRC (Fig. 8), their contribution was not major (Fig. 4(a)). In contrast, π-π interactions played an essential role in the adsorption process. This conclusion was supported by comparing the FTIR spectrum of H-SB before and after adsorption. Fig. 4(a) indicates a remarkable decrease in a band intensity at 1,430 cm^{-1} (involved in the C=C groups in H-SB) after adsorption, suggesting the existence of π-π interactions (Fig. 8) in adsorption mechanisms.

Some previous authors concluded the intermolecular forces of attraction (i.e., ion-dipole interaction) played an essential role in the adsorption process of aromatic pollutants onto the nano iron oxide-loaded materials. Such interaction can occur between the Fe atoms (or Cu atoms) on materials and the oxygen atoms of pollutants. For example, Leone et al. [14] investigated the adsorption mechanism between diclofenac drug and maghemite-based adsorbent.

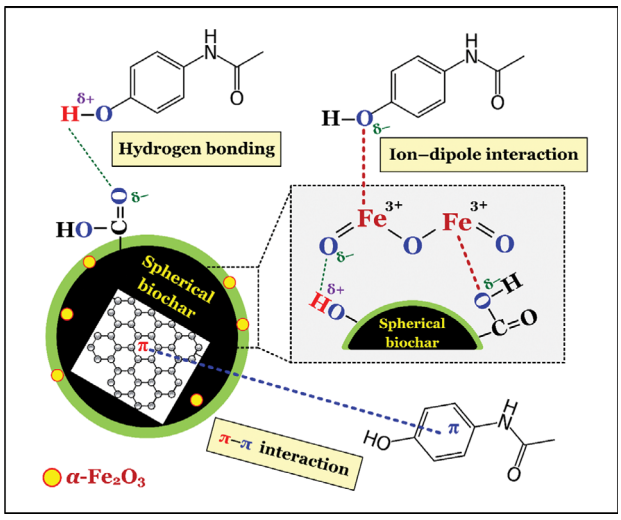

Fig. 8. Feasible mechanisms of PRC adsorption by hematite nanoparticles-loaded spherical biochar.

They concluded that ion-dipole interaction was regarded as one of the primary adsorption mechanisms. Similarly, this interaction has been reported by Dashamiri and co-workers [35] for adsorbing various organic dyes (auramine O, brilliant green, eosin yellow, and methylene blue dyes) by the CuO nanoparticle-loaded activated carbon. In this study, the existence of ion-dipole interaction (Fig. 8) might be identified by the FTIR technique. Fig. 4(a) shows a remarkable decrease in the band intensity of the C-O-Fe groups at 554 and 472 cm^{-1}.

In addition, Fig. 4(b) provides the key role of the presence of iron oxides in the adsorption process. After the oxidation process of H-SB using HNO_3, the adsorption capacity of H-SB substantially decreased because of the disappearance of the relevant C-O-Fe groups in Fig. 4(a). After the oxidation process, the band intensity at 1,050 cm^{-1} (C-O group) substantially increased. A similar increase in the intensity was also observed for the O-H group (3,450 cm^{-1}). The result again confirmed that the existence of nano iron oxides in the surface of H-SB resulted from the interaction between the C-O groups (and O-H groups) in the surface of H-SB and Fe atoms in hematite.

CONCLUSIONS

The α-Fe_2O_3 nanoparticle-loaded spherical biochar (H-SB) was directly prepared through the one-step pyrolysis process at the low temperature of 400 °C. The presence of iron solids on the surface of H-SB was observed by the SEM-EDS data. The XRD and Raman spectra confirmed that the dominant form of iron nanoparticles in H-SB was hematite (α-Fe_2O_3). The saturation magnetization of H-SB was 6.729 emu/g. The primary C-O and secondary O-H groups in H-SB played a critical role in keeping α-Fe_2O_3 nanoparticles in its surface. H-SB exhibited poor porosity (its S_{BET} of 127 m^2/g and V_{Total} of 0.089 cm^3/g) compared to activated carbon.

For the studies of PRC removal by H-SB, the adsorption process was affected slightly by pH solutions from 2 to 8 and reached a fast equilibrium at around 120 min. Its Langmuir maximum adsorption capacity at 30 °C and pH 7.0 was 49.9 mg/g, which was remarkably higher than its feedstock (0.15 mg/g) and pristine SB (3.51 mg/g). The adsorption was endothermic (ΔH^o=27.1 kJ/mol) within 283-298 K and exothermic (ΔH^o=−16.4 kJ/mol) within 298-323 K. The primary adsorption mechanism was ion-dipole interaction and π-π interaction; meanwhile, the minor contributions were hydrogen bonding and pore filling.

ACKNOWLEDGEMENTS

The study was supported by The Youth Incubator for Science and Technology Program, managed by Youth Development Science and Technology Center-Ho Chi Minh Communist Youth Union and Department of Science and Technology of Ho Chi Minh City, the contract number is "37/2020/HĐ-KHCNT-VU" (30/12/2020).

AUTHORS' CONTRIBUTION

Ton That Loc: Data Curation, Formal analysis, Project Admin-

istration. **Nguyen Duy Dat:** Formal analysis, Investigation, Writing - Review & Editing. **Hai Nguyen Tran:** Visualization, Validation, Funding acquisition, Project Administration, Supervision, Writing - Review & Editing. All authors read and approved the final manuscript.

SUPPORTING INFORMATION

Additional information as noted in the text. This information is available via the Internet at http://www.springer.com/chemistry/journal/11814.

REFERENCES

1. R. Bhateria and R. Singh, *J. Water Process. Eng.*, **31**, 100845 (2019).
2. S. M. Abdelbasir and A. E. Shalan, *Korean J. Chem. Eng.*, **36**, 1209 (2019).
3. I. Ihsanullah, *Chem. Eng. J.*, **388**, 124340 (2020).
4. P. Zhang, D. O'Connor, Y. Wang, L. Jiang, T. Xia, L. Wang, D. C. W. Tsang, Y. S. Ok and D. Hou, *J. Hazard. Mater.*, **384**, 121286 (2020).
5. M. Jain, M. Yadav, T. Kohout, M. Lahtinen, V. K. Garg and M. Sillanpää, *Water Resour. Ind.*, **20**, 54 (2018).
6. J. Kaur, M. Kaur, M. K. Ubhi, N. Kaur and J.-M. Greneche, *Mater. Chem. Phys.*, **258**, 124002 (2021).
7. H. N. Tran, F. Tomul, H. T. H. Nguyen, D. T. Nguyen, E. C. Lima, G. T. Le, C.-T. Chang, V. Masindi and S. H. Woo, *J. Hazard. Mater.*, **394**, 122255 (2020).
8. L. Yu, C. Falco, J. Weber, R. J. White, J. Y. Howe and M.-M. Titirici, *Langmuir*, **28**, 12373 (2012).
9. H. N. Tran, C.-K. Lee, T. V. Nguyen and H.-P. Chao, *Environ. Technol.*, **39**, 2747 (2018).
10. M. Sevilla and A. B. Fuertes, *Chem. Eur. J.*, **15**, 4195 (2009).
11. F.-C. Huang, C.-K. Lee, Y.-L. Han, W.-C. Chao and H.-P. Chao, *J. Taiwan. Inst. Chem. Eng.*, **45**, 2805 (2014).
12. A. Solanki and T. H. Boyer, *Chemosphere*, **218**, 818 (2019).
13. F. Tomul, Y. Arslan, B. Kabak, D. Trak and H. N. Tran, *J. Chem. Technol. Biotechnol.*, **96**, 869 (2021).
14. V. O. Leone, M. C. Pereira, S. F. Aquino, L. C. A. Oliveira, S. Correa, T. C. Ramalho, L. V. A. Gurgel and A. C. Silva, *New J. Chem.*, **42**, 437 (2018).
15. D. T. Nguyen, H. N. Tran, R.-S. Juang, N. D. Dat, F. Tomul, A. Ivanets, S. H. Woo, A. Hosseini-Bandegharaei, V. P. Nguyen and H.-P. Chao, *J. Environ. Chem. Eng.*, **8**, 104408 (2020).
16. A. L. Bursztyn Fuentes, R. L. S. Canevesi, P. Gadonneix, S. Mathieu, A. Celzard and V. Fierro, *Ind. Crops Prod.*, **155**, 112740 (2020).
17. S. Wong, Y. Lim, N. Ngadi, R. Mat, O. Hassan, I. M. Inuwa, N. B. Mohamed and J. H. Low, *Powder Technol.*, **338**, 878 (2018).
18. L. Spessato, K. C. Bedin, A. L. Cazetta, I. P. A. F. Souza, V. A. Duarte, L. H. S. Crespo, M. C. Silva, R. M. Pontes and V. C. Almeida, *J. Hazard. Mater.*, **371**, 499 (2019).
19. R. a. Markets, https://www.researchandmarkets.com/reports/4997604/paracetamol-market-growth-trends-covid-19 (2021).
20. S. Pandolfi, V. Simonetti, G. Ricevuti and S. Chirumbolo, *J. Med. Virol.*, **93**, 5704 (2021).
21. R. Cairns and J. A. Brown, *Med. J. Aust.*, **211**, 218 (2019).
22. W. J. Lee, P. S. Goh, W. J. Lau and A. F. Ismail, *Arab. J. Sci. Eng.*, **45**, 7109 (2020).
23. S. Y. Bunting, D. J. Lapworth, E. J. Crane, J. Grima-Olmedo, A. Koroša, A. Kuczyńska, N. Mali, L. Rosenqvist, M. E. van Vliet, A. Togola and B. Lopez, *Environ. Pollut.*, **269**, 115945 (2021).
24. B. Nunes, *Non-steroidal anti-inflammatory drugs in water: emerging contaminants and ecological impact*, Springer International Publishing, Cham (2020).
25. D. Spreitzer and J. Schenk, *Steel Res. Int.*, **90**, 1900108 (2019).
26. D. Cao, H. Li, L. Pan, J. Li, X. Wang, P. Jing, X. Cheng, W. Wang, J. Wang and Q. Liu, *Sci. Rep.*, **6**, 32360 (2016).
27. S. B. Kanungo and S. K. Mishra, *J. Therm. Anal.*, **46**, 1487 (1996).
28. L.-L. Sui, L.-N. Peng and H.-B. Xu, *Korean J. Chem. Eng.*, **38**, 498 (2021).
29. M. I. Dar and S. A. Shivashankar, *RSC Adv.*, **4**, 4105 (2014).
30. B. Ahmmad, K. Leonard, M. Shariful Islam, J. Kurawaki, M. Muruganandham, T. Ohkubo and Y. Kuroda, *Adv. Powder Technol.*, **24**, 160 (2013).
31. D. E. Fouad, C. Zhang, H. El-Didamony, L. Yingnan, T. D. Mekuria and A. H. Shah, *Results Phys.*, **12**, 1253 (2019).
32. P. J. Sephra, P. Baraneedharan, M. Sivakumar, T. D. Thangadurai and K. Nehru, *J. Mater. Sci.: Mater. Electron.*, **29**, 6898 (2018).
33. M. Tadic, D. Trpkov, L. Kopanja, S. Vojnovic and M. Panjan, *J. Alloys Compd.*, **792**, 599 (2019).
34. G. Ohemeng-Boahen, D. D. Sewu, H. N. Tran and S. H. Woo, *Colloids Surf. A*, **625**, 126911 (2021).
35. S. Dashamiri, M. Ghaedi, K. Dashtian, M. R. Rahimi, A. Goudarzi and R. Jannesar, *Ultrason. Sonochem.*, **31**, 546 (2016).
36. K. E. Waters, N. A. Rowson, R. W. Greenwood and A. J. Williams, *Sep. Purif. Technol.*, **56**, 9 (2007).
37. V. Ranjithkumar, S. Sangeetha and S. Vairam, *J. Hazard. Mater.*, **273**, 127 (2014).
38. V. Bernal, L. Giraldo and J. C. Moreno-Piraján, *Thermochim. Acta*, **683**, 178467 (2020).
39. D. Nematollahi, H. Shayani-Jam, M. Alimoradi and S. Niroomand, *Electrochim. Acta*, **54**, 7407 (2009).
40. M. Galhetas, M. A. Andrade, A. S. Mestre, E. Kangni-foli, M. J. Villa de Brito, M. L. Pinto, H. Lopes and A. P. Carvalho, *Phys. Chem. Chem. Phys.*, **17**, 12340 (2015).
41. I. C. Afolabi, S. I. Popoola and O. S. Bello, *Spectrochim. Acta A*, **243**, 118769 (2020).